Three-Dimensional Global Linear Stability Analysis of Flow Around a Spheroid

Asei Tezuka* and Kojiro Suzuki†
University of Tokyo, Tokyo 113-8656, Japan

Computational study of flowfields around a spheroid at varied angles of attack is done using Chiba's method, which is one of the methods of three-dimensional global linear stability analysis. It is clarified that in the case of a spheroid, nonoscillatory, nonaxisymmetric flow (in the case of zero angle of attack) and nonoscillatory asymmetric flow (in the case of nonzero angle of attack) are observed in a range of the freestream Reynolds number around 4×10^3 to 7×10^3, and angle of attack from 0 to 30 deg. The amplification factor of the nonoscillatory asymmetric (or nonaxisymmetric in 0-deg attack angle case) mode is the largest. The transition from nonoscillatory symmetric (or axisymmetric) flow, to nonoscillatory asymmetric (or nonaxisymmetric) flow, occurs when the amplification factor becomes zero. To ascertain the appearance of the nonoscillatory asymmetric flow in an attack angle case, a low-speed wind tunnel experiment was also conducted. The picture of flow visualization shows an asymmetric pattern when the Reynolds number is around 6.5×10^3, whereas the pattern is symmetric at a Reynolds number around 3.5×10^3.

Nomenclature

A = Jacobian matrix $\equiv \partial f(u_0)/\partial u$, where $\partial u/\partial t = f(u)$ satisfy the Navier–Stokes equations
B $\equiv \exp(AT)$
$c_{j,k}$ = coefficient of orthonormal basis ζ_j
f = frequency of oscillation
H = upper Hessenberg matrix whose elements are $c_{j,k}$
$\Im(\cdot)$ = imaginary part
i, j, k = radial, polar, and azimuthal cordinates
K_M = Krylov subspace $\equiv \text{span}\{\zeta_1, B\zeta_1, \dots, B^{M-1}\zeta_1\}$
M = size of the matrix H
N = number of grid points
$\Re(\cdot)$ = real part
Re = Reynolds number based on the diameter of sphere and the major axis of spheroid
Re_{C1} = critical Reynolds number from nonoscillatory axisymmetric (or symmetric in a nonzero attack angle case) flow to nonoscillatory planar symmetric (or asymmetric in a nonzero attack angle case) flow
Re_{C2} = critical Reynolds number from nonoscillatory flow to oscillatory flow
T = time to calculate the Navier–Stokes equations using initial conditions $u_0 + \varepsilon \zeta_i$ and $u_0 - \varepsilon \zeta_i$
T_{peri} = period of the oscillatory mode
t = time (nondimensionalized by freestream velocity and major axis length of spheroid)
u = column vector of velocity components at all of the computational nodes $\equiv (u_{1,1,1} v_{1,1,1} w_{1,1,1} \cdots$ $u_{i_{\max}, j_{\max}, k_{\max}} v_{i_{\max}, j_{\max}, k_{\max}} w_{i_{\max}, j_{\max}, k_{\max}})^T$
u_0 = stationary state of the velocity
$\tilde{u}$ = disturbance of velocity

$u_{i+}^{(\text{fin})}$ = velocity at time $t = T$ for the initial condition $u = u_{i+}^{(\text{ini})}$ at $t = 0$
$u_{i-}^{(\text{fin})}$ = velocity at time $t = T$ for the initial condition $u = u_{i-}^{(\text{ini})}$ at $t = 0$
$u_{i+}^{(\text{ini})}$ $\equiv u_0 + \varepsilon \zeta_i$
$u_{i-}^{(\text{ini})}$ $\equiv u_0 - \varepsilon \zeta_i$
ε = parameter to control the magnitude of disturbance
ζ_1 = starting vector of orthonormal basis made by random numbers
ζ_i = orthonormal basis of subspace K_M
λ = eigenvalue
$\lambda^{(A)}$ = approximate eigenvalue of matrix A
$\lambda^{(B)}$ = approximate eigenvalue of matrix B
$\lambda^{(H)}$ = eigenvalue of matrix H
$\varphi^{(A)}$ = approximate eigenvector of matrix A
$\varphi^{(B)}$ = approximate eigenvector of matrix B
$\psi^{(H)}$ = eigenvector of matrix H

Subscript

max = maximum

I. Introduction

TO understand the aerodynamics of a slender body at high angles of attack, it is necessary to investigate the structure of three-dimensional separation around the body. From an engineering viewpoint, investigation of the structure of a steady asymmetric flowfield is an important topic, because specific phenomena such as phantom yaw and flat spin are considered to be caused by the side force that is generated from a steady asymmetric flowfield.[1] Therefore, to investigate the condition that the nonoscillatory asymmetric flowfield becomes stable and the asymmetric flowfield generates side force is important. In this paper, we focus on the nonoscillatory asymmetric flow around a spheroid at an angle of attack in the range of Reynolds number $Re \sim 10^4$.

Figure 1 shows the schematic of the flowfield around a body in the critical Reynolds number range from steady flow to oscillatory flow. In the case of flow around a sphere, the appearance of a steady nonaxisymmetric flowfield has been pointed out in previous studies. Magarvey and Bishop[2] used dye visualization to reveal the wakes of free-falling drops of an immiscible liquid in water. If the flow is axisymmetric, the dye injected into the recirculating region converges to a single thread in the wake. The flow visualization result of Magarvey and Bishop[2] at $Re = 170$ (Re represent the Reynolds number based on the diameter and the freestream velocity), which is shown in Fig. 2a, demonstrates the single thread in wake. However, when

*Research Associate, Department of Aeronautics and Astronautics, School of Engineering, 7-3-1 Hongo, Bunkyo-ku. Member AIAA.
†Associate Professor, Department of Advanced Energy, Graduate School of Frontier Sciences, 7-3-1 Hongo, Bunkyo-ku. Member AIAA.
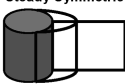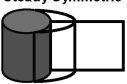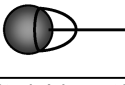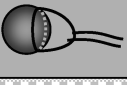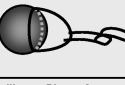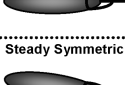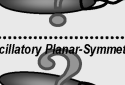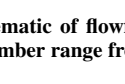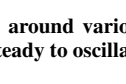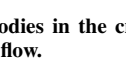
Fig. 1   Schematic of flowfields around various bodies in the critical Reynolds number range from steady to oscillatory flow.

a) **Single thread (*Re* = 170)**

b) **Double thread (*Re* = 220)**
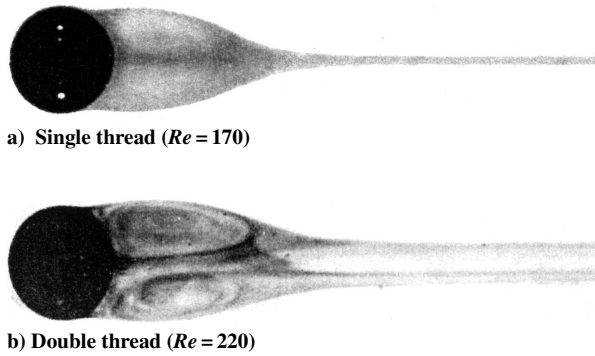
Fig. 2   Flow visualization results of Magarvey and Bishop.[2]

the Reynolds number is larger than a critical value $Re_{C1} \approx 210$, the dye converges to two parallel threads in the wake, which indicate that the flowfield is not axisymmetric (Fig. 2b). Oscillation of the double thread wake is observed in a Reynolds number region higher than $Re_{C2} \approx 270$.

It should be emphasized that there are two critical values in the transition region from steady flow to oscillatory flow. The first is the critical Reynolds number for transition from steady axisymmetric flow to steady nonaxisymmetric flow, and the second is the critical Reynolds number for transition from steady nonaxisymmetric flow to oscillatory flow. The appearance of nonoscillatory nonaxisymmetric flow has been illuminated in various studies. For example, Ormieres and Provansal[3] experimentally observed steady nonaxisymmetric flow, and Johnson and Patel[4] conducted both numerical and experimental studies and both results demonstrate the existence of the steady asymmetric flowfield.

In this study, we focus on the stability of such a nonoscillatory asymmetric flowfield using the application of a three-dimensional global linear stability analysis. As Theofilis[5] has explained, three-dimensional global linear flow instability research is based on the concept of a decomposition of any flow quantity into a steady or time-periodic laminar so-called basic flow, upon which small-amplitude three-dimensional disturbances are permitted to develop. Three spatial directions are resolved and time-periodic small-amplitude disturbances, inhomogeneous in all three directions, are superimposed upon a steady basic state, itself inhomogeneous in space. Therefore, the use of the term "global" is different from previous work of Huerre and Monkewitz,[6] who characterized a truly parallel flow in which the disturbance propagates upstream from its point of introduction as being globally unstable. In this paper, we use the term "global" from the viewpoint of Theofilis.

Natarajan and Acrivos[7] examined two-dimensional global linear stability of the flow around a sphere. Two-dimensional global lin-

ear stability calculates eigenmodes that are inhomogeneous in both the axial and radial directions and periodic in the azimuthal direction of cylindrical coordinates. The mechanism of the transition from steady axisymmetric flow to steady nonaxisymmetric flow in the critical Reynolds number region is explained. A nonoscillatory, nonaxisymmetric mode becomes dominant if the Reynolds number becomes larger than 210. Ghidersa and Dušek[8] calculated the two-dimensional global linear stability of the flow around a sphere, and the critical Reynolds number of the breakdown of the axial symmetry was calculated as $Re_{C1} \approx 212.2$. Ghidersa and Dušek pointed out that the appearance of the double-thread wake is explained by the superposition of the most unstable mode to the axisymmetric flowfield. Consequently, the existence of the nonoscillatory, nonaxisymmetric flow is described by the result of the global linear stability analysis.

If the shape of the body is changed from a sphere to a prolate spheroid, not only the Reynolds number, but also the angle of attack becomes an important parameter to determine the characteristics of the flowfield. In previous studies, it is reported that the separation pattern of the flowfield becomes complicated according to the increase in the angle of attack. Wang et al.[9] conducted a wind tunnel experiment for flow around a prolate spheroid whose length-to-diameter ratio was 4:1. The Reynolds number based on the diameter of the spheroid was 3.5×10^4. The pattern of the separation changes from closed separation to open separation according to the increase in the angle of attack. Han and Patel[10] performed an experimental study of flow around a spheroid whose length-to-diameter ratio was 4.3:1. The Reynolds number based on the length of the model was 8.0×10^4. This study also presents the change of the separation according to the increase in the angle of attack. The results of Costis et al.[11] and Nishikawa et al.[12] also demonstrate the pattern of surface streamlines of the flow around a spheroid at various angle of attack.

From the results for the sphere, it is expected that for a body with spheroidal shape, the flow may also become steady nonaxisymmetric in a certain range of a Reynolds number. However, the presence of nonoscillatory, nonaxisymmetric flow, or nonoscillatory asymmetric flow, has not been reported in the studies mentioned earlier. In this study, we demonstrate the appearance of nonoscillatory, nonaxisymmetric flow around a spheroid at zero angle of attack and nonoscillatory asymmetric flow around a spheroid at nonzero angle of attack.

The transition mode of the flow structure around a spheroid at nonzero angle of attack was examined by a three-dimensional global linear stability analysis. Chiba's method[13] was used to calculate the stability of the flowfield, because it can easily be coupled with the Navier–Stokes analysis by the finite-difference method on generalized coordinates. Three-dimensional flow around a sphere was analyzed to check the validity of our numerical code. The result was in desirable agreement with the result of Natarajan and Acrivos.[7] Following that, the three-dimensional global linear stability of flow around a spheroid at various angles of incidence was calculated. The effects of Reynolds number, angle of attack, and length-to-diameter ratio are discussed. To confirm the appearance of the nonoscillatory asymmetric flow, a low-speed wind tunnel experiment was also conducted under the condition of angle of attack 10 deg.

II.   Summary of Three-Dimensional Global Linear Stability Analysis

A.   Formulation

Theofilis[5] explained that three-dimensional global linear instability is decomposed as

$$\boldsymbol{q}(x, y, z, t) = \bar{\boldsymbol{q}}(x, y, z) + \varepsilon\hat{\boldsymbol{q}}(x, y, z)e^{-i\Omega t} \qquad (1)$$

with $\bar{\boldsymbol{q}}(x, y, z)$ and $\varepsilon\hat{\boldsymbol{q}}(x, y, z)e^{-i\Omega t}$ representing the steady basic flow and three-dimensional amplitude functions of the unsteady infinitesimal perturbations. Ω is a complex eigenvalue. In some papers, $\bar{\boldsymbol{q}}(x, y, z)$ is expressed as "base flow." In this paper, we follow the same manner as Theofilis.[5]

Chiba[11] has calculated three-dimensional global linear stability in the following way. The nondimensionalized incompressible laminar

Navier–Stokes equations

$$u_t + uu_x + vu_y + wu_z = -p_x + (u_{xx} + u_{yy} + u_{zz})/Re$$

$$v_t + uv_x + vv_y + wv_z = -p_y + (v_{xx} + v_{yy} + v_{zz})/Re$$

$$w_t + uw_x + vw_y + ww_z = -p_z + (w_{xx} + w_{yy} + w_{zz})/Re$$

$$p_{xx} + p_{yy} + p_{zz} = -u_x^2 - v_y^2 - w_z^2 - 2(u_y v_x + v_z w_y + w_z u_x)$$
$$+ (u_x + v_y + w_z)/\Delta t$$

can be summarized as

$$\frac{\partial \boldsymbol{u}}{\partial t} = \boldsymbol{f}(\boldsymbol{u}) \tag{2}$$

where

$$\boldsymbol{u} = \left(u_{1,1,1} v_{1,1,1} w_{1,1,1} \cdots u_{i_{max},j_{max},k_{max}} v_{i_{max},j_{max},k_{max}} w_{i_{max},j_{max},k_{max}}\right)^T$$

The expression of the function $\boldsymbol{f}(\boldsymbol{u})$ is very complicated. However, if we use Chiba's method, the three-dimensional global linear stability has been calculated without using the explicit expression of $\boldsymbol{f}(\boldsymbol{u})$. If the number of computational nodes ($i_{max} \times j_{max} \times k_{max}$) is N, the dimension of $\boldsymbol{u}$ becomes $3N$ in the three-dimensional case. Pressure is not included in the dependent variables, because it is independent of the velocity. A Taylor series expansion is applied to Eq. (2) around the stationary solution $\boldsymbol{u}_0$:

$$\boldsymbol{f}(\boldsymbol{u}_0 + \tilde{\boldsymbol{u}}) = \boldsymbol{f}(\boldsymbol{u}_0) + \frac{\partial \boldsymbol{f}(\boldsymbol{u}_0)}{\partial \boldsymbol{u}} \tilde{\boldsymbol{u}} + O(\tilde{\boldsymbol{u}}^2) \tag{3}$$

where $\tilde{\boldsymbol{u}}$ is a small disturbance. Considering that the second- or higher-order terms with respect to $|\tilde{\boldsymbol{u}}|$ are negligibly small, the linearized stability equation is given as

$$\frac{\partial \tilde{\boldsymbol{u}}}{\partial t} = \frac{\partial \boldsymbol{f}(\boldsymbol{u}_0)}{\partial \boldsymbol{u}} \tilde{\boldsymbol{u}} \equiv \boldsymbol{A}\tilde{\boldsymbol{u}} \tag{4}$$

where $\boldsymbol{A} \equiv \partial \boldsymbol{f}(\boldsymbol{u}_0)/\partial \boldsymbol{u}$ is the Jacobian matrix.

Substituting the eigenvalue λ and eigenvector φ of matrix $\boldsymbol{A}$ into Eq. (4), we obtain

$$\frac{\partial \varphi}{\partial t} = \lambda \varphi \tag{5}$$

If $\tilde{\boldsymbol{u}}(0)$ can be expressed by a linear combination of eigenvectors φ_n so that $\tilde{\boldsymbol{u}}(0) = \sum k_n \varphi_n$, then $\tilde{\boldsymbol{u}}(t)$ satisfies

$$\tilde{\boldsymbol{u}}(t) = \sum k_n \varphi_n \exp(\lambda_n) \tag{6}$$

We can evaluate the three-dimensional global linear stability of flow by the real part of λ [i.e., $\Re(\lambda)$]. The mode of velocity disturbance is represented by φ. If the real part of the eigenvalue is positive or negative, then the magnitude of the mode is growing (the flow is unstable) or diminishing (the flow is stable), respectively. The frequency of the oscillatory mode is evaluated by the imaginary part of λ [i.e., $\Im(\lambda)$]. If the imaginary part of the eigenvalue is zero or nonzero, the mode is steady or oscillatory, respectively.

B. Numerical Method

The three-dimensional global linear stability is analyzed by considering the eigensystem of Eq. (4). However, the size of matrix $\boldsymbol{A}$ is $3N \times 3N$, and it is difficult to calculate the eigensystem of matrix $\boldsymbol{A}$. Chiba[13] adopted Eriksson and Rizzi's method[14] to determine the critical Reynolds number in the case of a circular cylinder and obtained reasonable results. In his approach, Arnoldi's method[15] was used to calculate the eigenvalue analysis of matrix $\boldsymbol{A}$ approximately. The flowchart of Chiba's method is demonstrated in Fig. 3.

By integrating Eq. (4) with respect to time from 0 to T, we obtain

$$\tilde{\boldsymbol{u}}(T) = \exp(\boldsymbol{A}T)\tilde{\boldsymbol{u}}(0) \tag{7}$$

Give initial normalized disturbance $\boldsymbol{\zeta}_1$ by random numbers.

for k=1 to M:

Calculate Navier-Stokes equations while T using a pair of initial values, $\boldsymbol{u}_0 + \varepsilon \boldsymbol{\zeta}_k$, and $\boldsymbol{u}_0 - \varepsilon \boldsymbol{\zeta}_k$. The results are written as: $\boldsymbol{u}_{k+}$, and $\boldsymbol{u}_{k-}$.

$$\boldsymbol{B}\boldsymbol{\zeta}_k = (\boldsymbol{u}_{k+} - \boldsymbol{u}_{k-})/2\varepsilon$$

$$\tilde{\boldsymbol{u}}_{k+1} = \boldsymbol{B}\boldsymbol{\zeta}_k - \sum_{j=1}^{k} h_{j,k}\boldsymbol{\zeta}_j \; ; \quad h_{j,k} = \boldsymbol{\zeta}_j^T \cdot \boldsymbol{B}\boldsymbol{\zeta}_k$$
$$h_{k+1,k} = (\tilde{\boldsymbol{u}}_{k+1}^T \cdot \tilde{\boldsymbol{u}}_{k+1})^{1/2}$$
$$\boldsymbol{\zeta}_{k+1} = \tilde{\boldsymbol{u}}_{k+1} / h_{j+1,k}$$

next k

Calculate eigenvalues $\lambda^{(H)}$ and eigenvectors $\boldsymbol{\psi}^{(H)}$ of $\boldsymbol{H}$.

$\lambda^{(B)} = \lambda^{(H)}$, $\boldsymbol{\varphi}^{(B)} = \{\boldsymbol{\zeta}_1, ..., \boldsymbol{\zeta}_k\} \boldsymbol{\psi}^{(H)}$.

$\lambda^{(A)} = \{ \log|\lambda^{(B)}| + i \arg \lambda^{(B)}\}/T$, $\boldsymbol{\varphi}^{(A)} = \boldsymbol{\varphi}^{(B)}$.
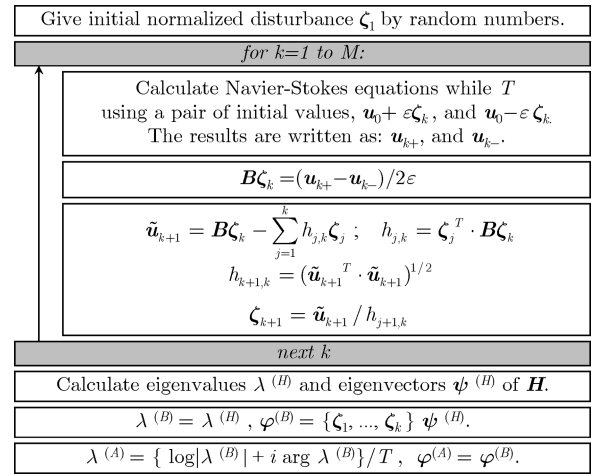
Fig. 3 Flowchart of the Chiba method.

The approximate eigensystem of $\boldsymbol{B}[\equiv \exp(\boldsymbol{A}T)]$ is numerically calculated by Arnoldi's method. The eigensystem of matrix $\boldsymbol{A}$ is easily calculated if we obtain an eigensystem of matrix $\boldsymbol{B}$. The approximate eigensystem of matrix $\boldsymbol{B}$ is expressed by a vector that is in the Krylov subspace $K_M = \text{span}\{\zeta_1, \boldsymbol{B}\zeta_1, \ldots, \boldsymbol{B}^{M-1}\zeta_1\}$. The normalized orthogonal basis vectors of subspace K_M, which are written as ζ_i ($1 \leq i \leq M$, $M \ll N$), are introduced. ζ_i is a column vector and the number of elements are $3N$. The vector ζ_i is given by random numbers. To obtain the basis vector ζ_i ($2 \leq i \leq M$), the Gram–Schmidt orthogonalization method is used. Suppose that $\boldsymbol{B}\zeta_1$ is expressed by the linear combination of the orthogonal bases ζ_1 and ζ_2. Then ζ_2 is specified by the orthonormal condition. In order to calculate the $\boldsymbol{B}\zeta_1$, ζ_1 is assigned to $\tilde{\boldsymbol{u}}(0)$ of Eq. (7). Thus, $\tilde{\boldsymbol{u}}(T)$ corresponds to $\boldsymbol{B}\zeta_1$.

It should be emphasized that in Chiba's method, the stability of the flowfield is calculated by adding small disturbances to the converged solution of computational fluid dynamics (CFD), and then time evolutions were solved using the same CFD schemes. In this paper, the stability is calculated under the subcritical condition. The converged solution of the Navier–Stokes equations, which is expressed as $\boldsymbol{u}_0$, is used as a basic flow of the stability analysis. The basic flows are different in different Reynolds numbers.

From Eq. (7), we can say that $\tilde{\boldsymbol{u}}(0)$ is a disturbance vector at $t = 0$, and $\tilde{\boldsymbol{u}}(T)$ is a disturbance vector at $t = T$. Therefore, the Navier–Stokes equations are solved from $t = 0$ to $t = T$ using the initial value which contains the velocity disturbance ζ_1. Two types of initial values, $\boldsymbol{u}_{i+}^{(\text{ini})}(\equiv \boldsymbol{u}_0 + \varepsilon \zeta_1)$ and $\boldsymbol{u}_-^{(\text{ini})}(\equiv \boldsymbol{u}_0 - \varepsilon \zeta_1)$, are used to solve the Navier–Stokes equations. The result at $t = T$ are written as $\boldsymbol{u}_{i+}^{(\text{fin})}$ and $\boldsymbol{u}_{i-}^{(\text{fin})}$, respectively. The vector $\boldsymbol{B}\zeta_1[= \exp(\boldsymbol{A}T)\zeta_1]$ is calculated from the following equation:

$$\boldsymbol{B}\zeta_1 = \left(\boldsymbol{u}_{1+}^{(\text{fin})} - \boldsymbol{u}_{1-}^{(\text{fin})}\right)/2\varepsilon \tag{8}$$

The number of elements of vector ζ_i is $3N$, and ζ_i satisfies the normalized condition $|\zeta_i| = 1$. The component of ζ_i becomes small if the number of elements $3N$ is large. Because N is the number of grid points, the magnitude of disturbance at each computational node is affected by the size of computational mesh. Then, the parameter ε is introduced.

The vector ζ_2 is introduced to describe the vector $\boldsymbol{B}\zeta_1$ using a set of orthonormal basis ζ_i and ζ_2:

$$\boldsymbol{B}\zeta_1 = c_{1,1}\zeta_1 + c_{2,1}\zeta_2$$

The vectors $\zeta_3, \zeta_4, \ldots, \zeta_M$ are calculated in the same way.

First, the vector $\boldsymbol{B}\zeta_i$ is calculated from the equation

$$\boldsymbol{B}\zeta_1 = \left(\boldsymbol{u}_{1+}^{(\text{fin})} - \boldsymbol{u}_1^{(\text{fin})}\right)/2\varepsilon$$

Next, the vector ζ_{i+1} is introduced:

$$\boldsymbol{B}\zeta_i = c_{1,i}\zeta_1 + c_{2,i}\zeta_2 + \cdots + c_{j,i}\zeta_j + \cdots + c_{i+1,i}\zeta_{i+1} \tag{9}$$

Gram–Schmidt orthogonalization was applied to calculate ζ_{i+1}. The coefficient $c_{j,i}$ of orthonormal basis $\zeta_j (1 \leq j \leq i)$ is calculated as

$$c_{j,i} = \zeta_j^T \cdot \boldsymbol{B}\zeta_i \tag{10}$$

Then, $c_{i+1,i}\zeta_{i+1}$ is calculated from the following relation:

$$c_{i+1,i}\zeta_{i+1} = \boldsymbol{B}\zeta_i - (c_{1,i}\zeta_1 + c_{2,i}\zeta_2 + \cdots + c_{i,i}\zeta_i) \tag{11}$$

$c_{i+1,i}$ and ζ_{i+1} are calculated from the equations

$$c_{i+1,i} = (c_{i+1,i}\zeta_{i+1} \cdot c_{i+1,i}\zeta_{i+1})^{\frac{1}{2}} \tag{12}$$

$$\zeta_{i+1} = (c_{i+1,i}\zeta_{i+1})/c_{i+1,i} \tag{13}$$

At the end of the calculation, the following equation is obtained:

$$\boldsymbol{B}\zeta_M = c_{1,M}\zeta_1 + c_{2,M}\zeta_2 + \cdots + c_{j,M}\zeta_j + \cdots + c_{M,M}\zeta_M + c_{M+1,M}\zeta_{M+1} \tag{14}$$

In the case in which M is large and $|c_{M+1,M}\zeta_{M+1}|$ is small, we can approximate Eq. (14) as

$$\boldsymbol{B}\zeta_M = c_{1,M}\zeta_1 + c_{2,M}\zeta_2 + \cdots + c_{j,M}\zeta_j + \cdots + c_{M,M}\zeta_M \tag{15}$$

The coefficient $c_{j,k}$ and basis vector ζ_j satisfy

$$\boldsymbol{B}\{\zeta_1, \ldots, \zeta_M\} = \{\zeta_1, \ldots, \zeta_M\}\underbrace{\begin{bmatrix} c_{1,1} & \cdots & \cdots & c_{1,M-1} & c_{1,M} \\ c_{2,1} & \cdots & \cdots & c_{2,M-1} & c_{1,M} \\ 0 & \ddots & & \vdots & \vdots \\ \vdots & \ddots & \ddots & \vdots & \vdots \\ 0 & \cdots & 0 & c_{M,M-1} & c_{M,M} \end{bmatrix}}_{H} \tag{16}$$

The $M \times M$ matrix $\boldsymbol{H}$ whose elements are $c_{j,k}$ is obtained. The eigensystem of $\boldsymbol{B}$ is approximately calculated from the eigensystem analysis of the matrix $\boldsymbol{H}$ of size $M \times M$ instead of the matrix $\boldsymbol{B}$ of size $3N \times 3N$. Considering that the eigenvalue $\lambda^{(H)}$ and eigenvector $\psi^{(H)}$ of matrix $\boldsymbol{H}$ satisfies the equation

$$\boldsymbol{H}\psi^{(H)} = \lambda^{(H)}\psi^{(H)}$$

Eq. (16) becomes

$$\boldsymbol{B}\{\zeta_1, \ldots, \zeta_M\}\psi^{(H)} = \{\zeta_1, \ldots, \zeta_M\}\boldsymbol{H}\psi^{(H)}$$

$$= \{\zeta_1, \ldots, \zeta_M\}\lambda^{(H)}\psi^{(H)}$$

$$= \lambda^{(H)}\{\zeta_1, \ldots, \zeta_M\}\psi^{(H)} \tag{17}$$

Therefore the eigenvalue $\lambda^{(H)}$ of matrix $\boldsymbol{H}$ is an approximate eigenvalue of matrix $\boldsymbol{B}$. The vector $\{\zeta_1, \ldots, \zeta_M\}\psi^{(H)}$ becomes the approximate eigenvector of matrix $\boldsymbol{B}$. The approximate eigenvalue $\lambda^{(B)}$ and eigenvector $\varphi^{(B)}$ of matrix $\boldsymbol{B}$ are calculated from Eqs. (18) and (19):

$$\lambda^{(B)} = \lambda^{(H)} \tag{18}$$

$$\varphi^{(B)} = \{\zeta_1, \ldots, \zeta_M\}\psi^{(H)} \tag{19}$$

The eigenvalue $\lambda^{(A)}$ of the matrix $\boldsymbol{A}$ is obtained by the relation

$$\lambda^{(B)} = \exp\left(\lambda^{(A)}T\right) \tag{20}$$

The eigenvector $\varphi^{(A)}$ for the system $\boldsymbol{A}$ is the same as that for system $\boldsymbol{B}$:

$$\varphi^{(A)} = \varphi^{(B)} \tag{21}$$

C. Computational Conditions

For accurate evaluation of the stability of the flow, M must be sufficiently large. According to the increase in M, eigenvalues and eigenvectors obtained by Arnoldi's method converged to the exact solution. In this study, we focus on the most amplified mode, whose value of $\Re(\lambda^{(A)})$ is larger than those of other modes. It should be noted that in Arnoldi's method, more amplified modes with a larger real part of the eigenvalue are computed more accurately than the lesser amplified modes. In this study, M is set as 40. We have checked that if M is larger than 40, the configuration of the velocity disturbance of the most amplified mode becomes almost the same.

In this paper, we set the value of T as 1. Using Chiba's method, the stability of flow is calculated in the subcritical condition. The velocity disturbances of all modes decay in this condition. If T is larger than a half period of oscillation, an aliasing-like problem occurs. The eigenvalue $\lambda^{(A)}$ of the matrix $\boldsymbol{A}$ is calculated by Eq. (20) as

$$\lambda^{(A)} = \left\{\log\left|\lambda^{(B)}\right| + i \arg \lambda^{(B)}\right\}\Big/T \tag{22}$$

The natural logarithm function is a multivalued function, and we cannot determine the imaginary part of $\lambda^{(A)}$. To deal with this aliasing-like problem, the numerical simulation of the flowfield is also conducted at a supercritical Reynolds number. We can estimate the value of $\lambda^{(A)}$ by comparing the frequency of the oscillation observed in the CFD results at the supercritical condition.

The variable ε of Eq. (8) is introduced to control the magnitude of the velocity disturbance at each grid point. Because of the limit of the number of bits in representing numbers, a round-off error appears if $\varepsilon\zeta_i$ is very small compared to $\boldsymbol{u}_0$. If ε is too large, the higher-order term in Eq. (3) becomes large and we cannot neglect the higher-order term. In out trial computation, there is no significant difference between the results for $\varepsilon = 1$ and 0.01. In this study, we set ε to be 1.

The marker-and-cell method[16] was used to solve the Navier–Stokes equations. The Poisson equation for pressure was solved by the successive over relaxation method. The second-order Adams–Bashforth method was used for time integration. Artificial viscosity was introduced to calculate the flowfield. To check the influence of the numerical viscosity, which is applied to the convection terms, the third-order upwind finite-difference[17] and Kawamura–Kuwahara scheme[18] are applied in the trial computation. By comparing those results, we can estimate the influence of the numerical viscosity. The value of $\lambda^{(A)}$ calculated using the Kawamura–Kuwahara scheme becomes smaller than that calculated by using third-order upwind finite difference. However, the eigenvector φ, which demonstrates the configuration of the velocity disturbance of the mode, is almost the same. The effect of numerical viscosity is not essential in discussing the appearance of the nonoscillatory asymmetric flow. In this study, the third-order upwind finite difference is applied.

The grid is O–O type around the body, as shown in Fig. 4. The number of grid points is $51 \times 41 \times 51$. To confirm the appearance of the nonoscillatory asymmetric flow, the flow is also solved using a finer grid ($81 \times 61 \times 61$) in some computational conditions. In both cases, the flowfield becomes nonoscillatory and asymmetric.

At the outer boundary, the freestream boundary condition and zeroth-order extrapolation are applied at the inflow and outflow boundaries, respectively. At the inflow boundary the value of $\boldsymbol{u}$ is fixed to the freestream velocity. Assuming that the velocity disturbance $\tilde{\boldsymbol{u}}$ is added to the stationary solution $\boldsymbol{u}_0$ and solved in the same way to calculate the basic flow, the value of $\tilde{\boldsymbol{u}}$ is fixed to zero. At the outflow boundary, zeroth-order extrapolation is applied to the value of $\boldsymbol{u}$. In this case, the value of $\tilde{\boldsymbol{u}}$ also fulfills the zeroth-order extrapolation condition.

The distance from the surface of the body to the outer boundary is 20 times the length of the major axis. To check the validity of the distance, a trial computation is also conducted using a different type of numerical grid.
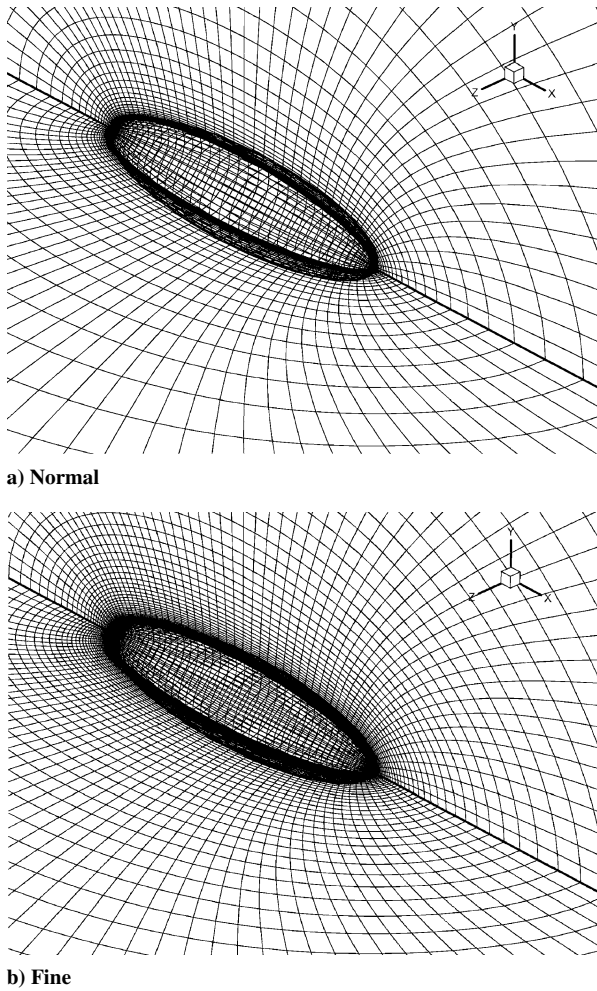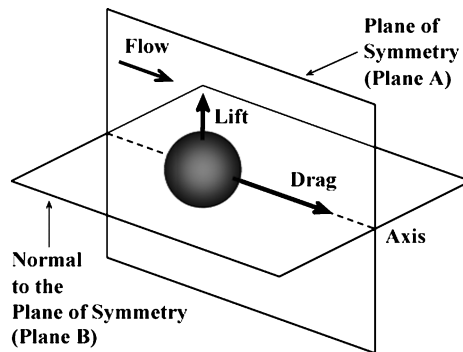
a) Normal

b) Fine

Fig. 4   Computational grid.

Fig. 5   Definition of the planes and forces (flow around a sphere).

a) Axisymmetric flow ($Re = 200$)

Double-Thread Wake

b) Nonaxisymmetric flow ($Re = 250$)

Fig. 6   Streamline of the flow around a sphere.

Fig. 7   Eigenvalues on a complex plane (sphere, $Re = 220$).

III.   Numerical Results and Discussion

A.   Flow Around a Sphere

To check the validity of our numerical code, three-dimensional flow around a sphere was analyzed and the result is compared to other studies. Figure 5 explains the definition of the planes and forces used in the following discussion. Our CFD results are shown in Fig. 6. The streamlines, which are plotted from the surface of the sphere, converge to two threads in the wake of the sphere at $Re = 250$ (Fig. 6b), whereas the streamlines converge to one thread in the wake of the sphere at $Re = 200$.

The eigenvalues of modes at $Re = 200$ calculated by the stability analysis are plotted on the complex plane in Fig. 7. The steady-state solution of the Navier–Stokes equations at $Re = 200$ (Fig. 6a) is selected as the basic flow. The mode shown by an arrow in the figure has the largest real part of the eigenvalue (which represents
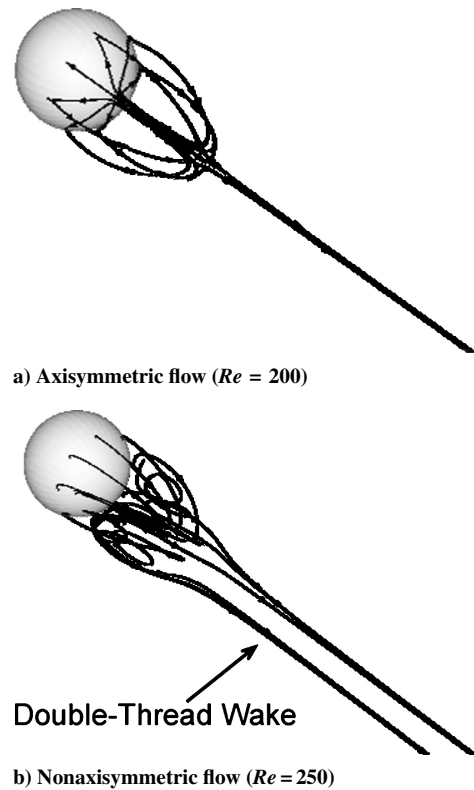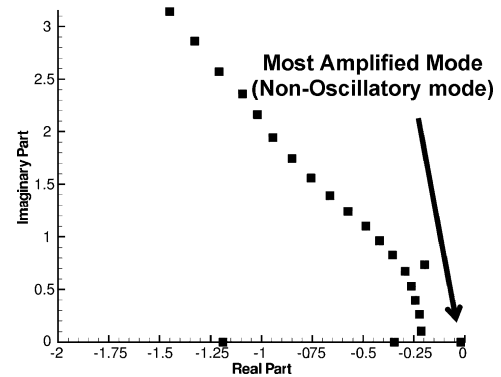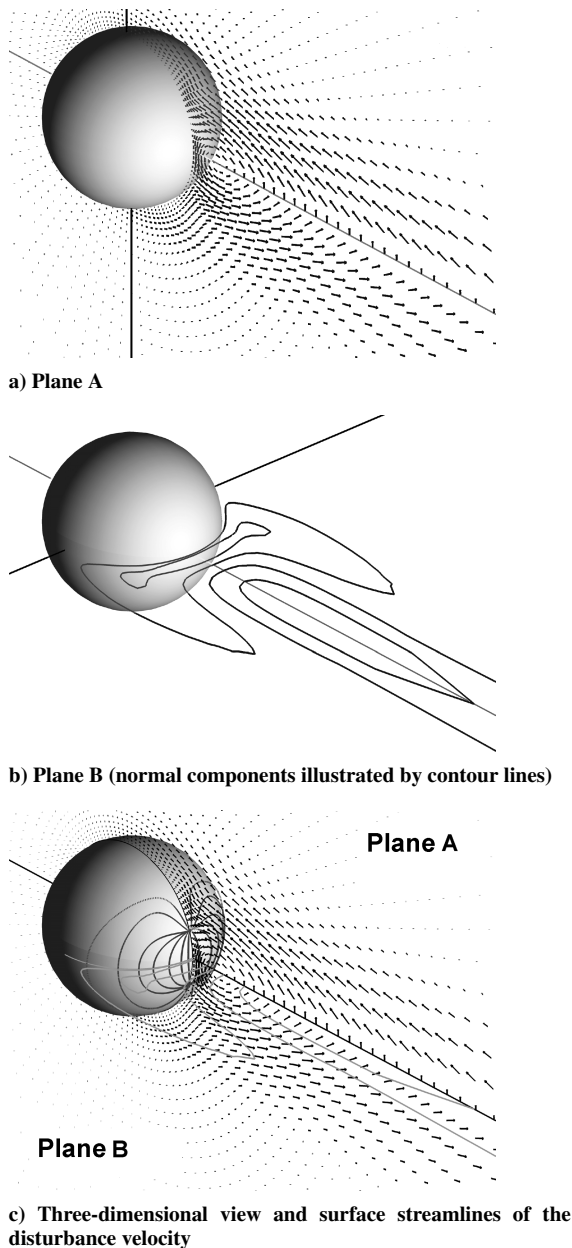
the amplification factor). This mode is determined to be the most amplified mode. The imaginary part of the most amplified mode (which represents the angular frequency) is zero. Therefore, this mode is a nonoscillatory mode. Figure 8 shows the vector disturbances of the most amplified mode. The cross-sectional view of the vector disturbances in the plane of symmetry (corresponding to plane A in Fig. 5) is plotted in Fig. 8a. All of the components of the disturbance vector are parallel to this plane. This result satisfies the condition that normal components should be zero in a symmetric plane. Figure 8b shows the vector disturbance on plane B. All of the components of the vector disturbance are normal to plane B, and the magnitude of the vector disturbance is plotted by contour lines. A three-dimensional plot of the vector disturbance is plotted in Fig. 8c. In the vicinity of the surface of a sphere (one grid point away from the surface), the streamlines of the vector disturbance are plotted. To draw the surface streamline, the component of vector disturbance that is parallel to the surface is integrated. This pattern is not axisymmetric but planar-symmetric.
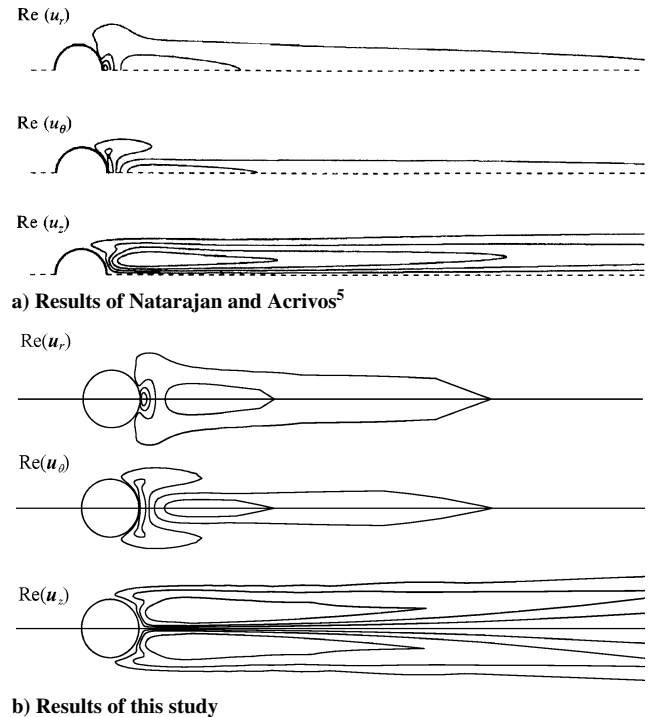
Natarajan and Acrivos[7] calculated two-dimensional global linear stability of the flow around a sphere, whose eigenmodes are inhomogeneous in both z (axial) and r (radial), and periodic in the θ (azimuthal) direction. The pattern of the eigenmode calculated by
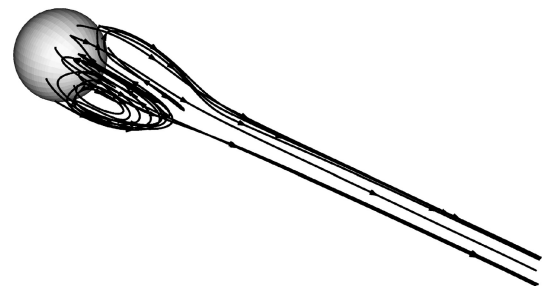
a) Plane A

b) Plane B (normal components illustrated by contour lines)

c) Three-dimensional view and surface streamlines of the disturbance velocity

Fig. 8   Distribution of the velocity disturbance of the most unstable mode (sphere, $Re = 220$).

a) Results of Natarajan and Acrivos[5]

b) Results of this study

Fig. 9   Comparison with results of Natarajan and Acrivos.[5]

Fig. 10   Streamline of velocity when the most amplified mode is superposed on the basic flow.

Natarajan and Acrivos,[5] which is shown in Fig. 9, is in desirable agreement with our result, which is plotted in the way of Natarajan and Acrivos. The flow around a sphere becomes nonaxisymmetric when the Reynolds number is larger than 210. The result of our numerical code shows that the critical Reynolds number Re_{C1} is around 226. The value of the critical Reynolds number that is calculated numerically is affected by the numerical viscosity. If we use a finer grid ($71 \times 41 \times 51$), the critical value becomes $Re_{C1} = 213$, whose value is close to the result of Natarajan and Acrivos. In both cases, the configuration of the velocity disturbance is the same.

Supposing that a nonaxisymmetric velocity disturbance field is added to the axisymmetric velocity field, the flowfield changes from axisymmetric to nonaxisymmetric. Then, if the eigenvalue becomes positive according to the increase in the Reynolds number, the flowfield changes from axisymmetric to nonaxisymmetric. The imaginary part of the eigenvalue is zero, and the mode is nonoscillatory. Therefore, a transition of flow from nonoscillatory axisymmetric to nonoscillatory nonaxisymmetric occurs. Ghidersa and Dušek[8] has explained the appearance of the double-thread wake by the fact that if the mode is superposed on the basic flow, there appear two loci of convergence points in the transverse flowfield. In this study, to il-

lustrate the transformation of the flowfield, the disturbance vectors are superposed on the basic flow. The flowfield shown in Fig. 10 demonstrates the streamlines, which converge to two threads in the wake.

B.   Flow Around a Spheroid
1.   Angle of Attack of 0 deg
First, the flow around a spheroid was numerically calculated. The incompressible Navier–Stokes equations are nondimensionalized with the major axis of the spheroid and magnitude of the uniform flow. Considering that the length-to-diameter ratio of the prolate spheroid is 4:1, the diameter of the spheroid becomes 0.25. The definition of the planes and forces used in the following discussion is shown in Fig. 11. The angle of attack is defined as the angle between the flow direction and the major axis. Figure 12 shows the surface streamlines of the flowfield around a spheroid. The pattern of the surface streamline at $Re = 3.5 \times 10^3$, which is shown in Fig. 12a, is axisymmetric. Figure 12b shows the surface streamlines at $Re = 5.0 \times 10^3$. The pattern of the surface streamlines becomes nonaxisymmetric. This nonaxisymmetric flowfield is also confirmed by the force acting on the body. The time history of the lift-to-drag force at $Re = 5.0 \times 10^3$ is shown in Fig. 12c. Because the normal force is generated on the body, the flowfield at $Re = 5.0 \times 10^3$ is not axisymmetric. The critical Reynolds number from symmetric flow to asymmetric flow exists between $Re = 3.5 \times 10^3$ and $Re = 5.0 \times 10^3$.

The stability of the flow around a spheroid was calculated. The stationary solution of CFD results at each Reynolds number (similar to
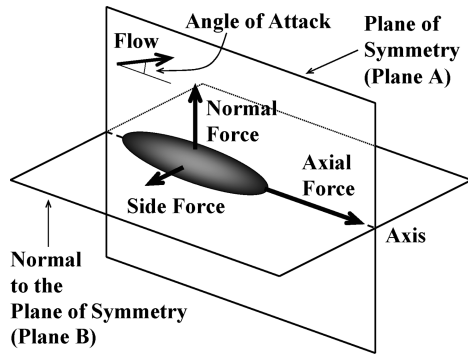
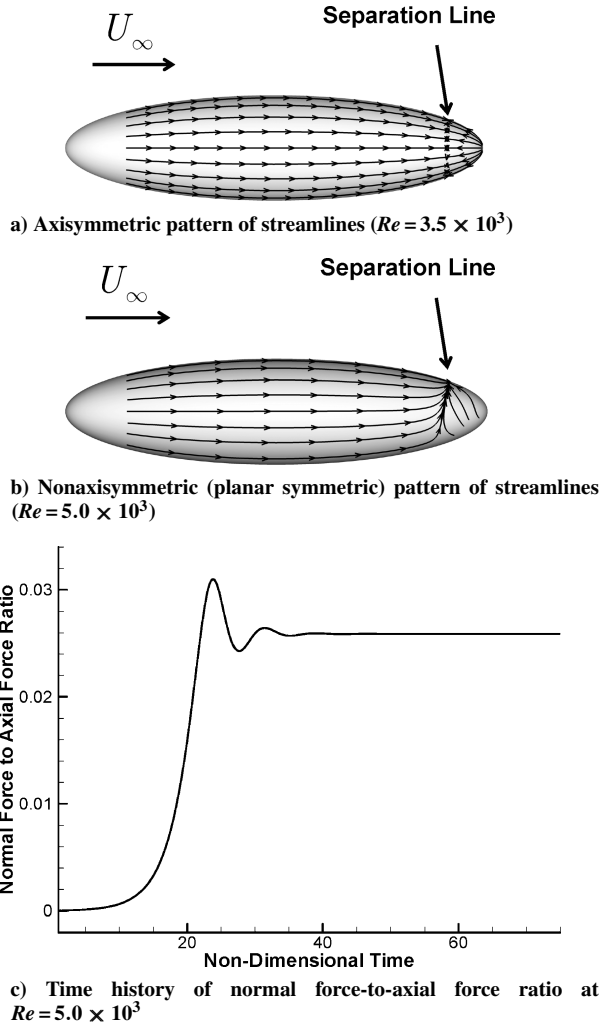Fig. 11 Definition of the planes and forces (spheroid).

a) Axisymmetric pattern of streamlines ($Re = 3.5 \times 10^3$)

b) Nonaxisymmetric (planar symmetric) pattern of streamlines ($Re = 5.0 \times 10^3$)

c) Time history of normal force-to-axial force ratio at $Re = 5.0 \times 10^3$

Fig. 12 CFD results for flow past a spheroid (angle of attack = 0 deg).

Fig. 13 Eigenvalues on a complex plane (spheroid, angle of attack = 0 deg, $Re < Re_{c1}$).

Fig. 14 Distribution of velocity disturbance of the most amplified mode (spheroid, angle of attack = 0 deg, $Re = 3.7 \times 10^3$).

Fig. 15 Time history of the lift-to-drag ratio (spheroid, angle of attack = 0 deg).

Fig. 12a) is used as the basic flows of the stability analysis. Figure 13 shows the eigenvalues in the complex plane. The mode that has the largest real part of the eigenvalue is the most amplified mode. In the $Re = 3.7 \times 10^3$ case, which is denoted by the inverted triangle, the imaginary part of the eigenvalue for the most amplified mode is zero. This mode is a nonoscillatory mode. The real parts of the eigenvalues for the oscillatory modes, whose imaginary parts of eigenvalues are not zero, are smaller than the nonoscillatory mode. Therefore, the oscillatory modes attenuate faster than the nonoscillatory mode.

Figure 14 shows the vector disturbance of the nonoscillatory mode in the case $Re = 3.7 \times 10^3$. Every vector disturbance on plane A is parallel to the plane, and the normal components of the disturbance vectors are approximately zero. In plane B, every vector disturbance is normal to the plane. The normal components of the vectors are represented by contour lines. We have checked the whole flowfield
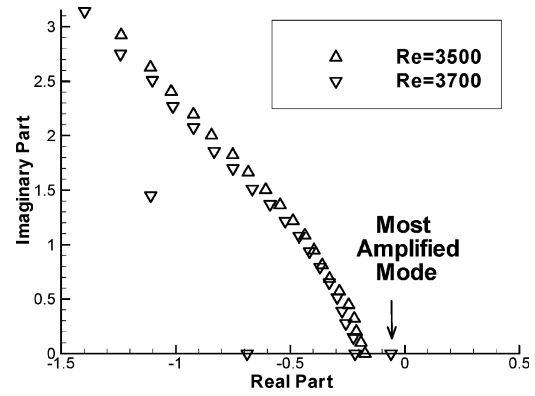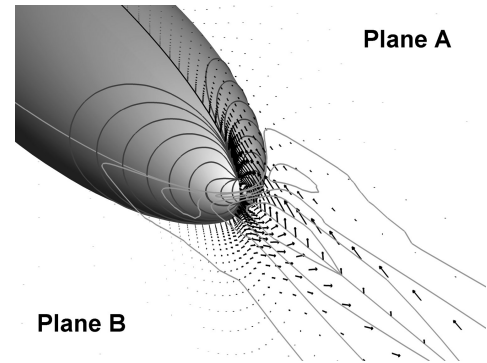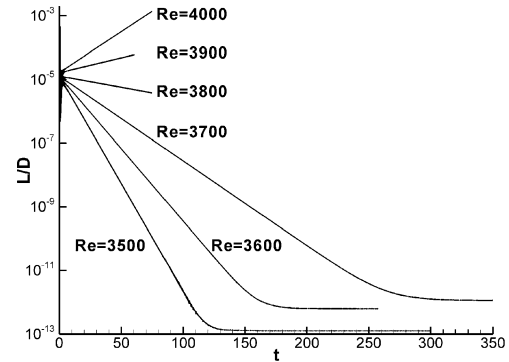
and confirmed that the velocity disturbance of the most amplified mode satisfies the planer symmetric condition. The result of Fig. 14 is almost the same as the result of the flow around a sphere (Fig. 8c). Figure 14 also presents the three-dimensional view of the surface streamline, which is plotted in the same way as Fig. 8c. The pattern of Fig. 14 resembles the pattern of Fig. 8. This result demonstrates that the structure of the velocity disturbance of the nonaxisymmetric mode is almost the same for the sphere and spheroid at zero attack angles.

From the result in Fig. 13, we can estimate that according to the increase in the Reynolds number, the real part of the nonoscillatory mode increases and becomes zero when the flowfield is neutral stable. If the Reynolds number becomes larger than the critical Reynolds number Re_{C1}, the transition from nonoscillatory axisymmetric flow to nonoscillatory, nonaxisymmetric flow, occurs. This value is estimated as 3.84×10^3.

If the Reynolds number is close to Re_{C1}, the damping ratio of the nonoscillatory nonaxisymmetric mode becomes close to zero. The time histories of the CFD results at various Reynolds numbers are plotted in Fig. 15. If the Reynolds number is close to the critical
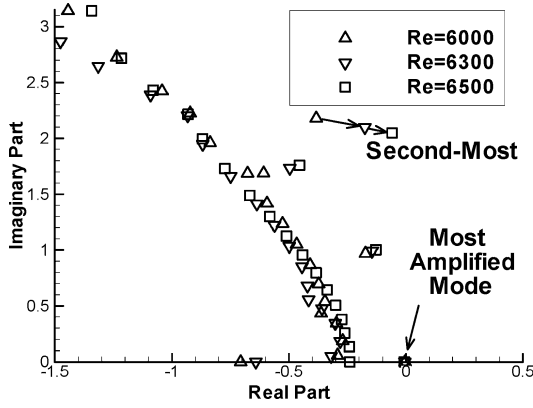
Fig. 16 Eigenvalues on a complex plane (spheroid, angle of attack = 0 deg, $Re_{c1} < Re < Re_{c2}$).

Reynolds number, the gradient of Fig. 15 becomes close to zero. This result implies that at a long time from the beginning of the computation, only the nonaxisymmetric mode that determines the transition exists in the flowfield. In fact, the gradient of the time history of the normal-force-to-axial-force ratio in Fig. 15 is consistent with the amplification factor obtained by stability analysis. Thus, we can calculate the critical value Re_{C1} by the condition that the gradient in Fig. 15 becomes zero. In the following section, the critical value Re_{C1} is estimated by the time history of the CFD results.

To check the dependency of the critical value Re_{C1} on the grid resolution, Re_{C1} is calculated by this way of using a fine grid. The critical value is 3.83×10^3, which is essentially the same as the value of the normal grid. The dependency of the value Re_{C1} on the grid resolution is low.

From the result of flow around a sphere, we can expect that the critical Reynolds number Re_{C2} from nonoscillatory flow to oscillatory flow also exists. The stability is also calculated under the condition that the Reynolds number is larger than 3.84×10^3. The converged solution of CFD, whose flowfield demonstrates the nonaxisymmetric flow pattern (similarly to Fig. 12b), is used as the basic flow. The result is shown in Fig. 16. In each case ($Re = 6.0 \times 10^3$ and 6.5×10^3) the imaginary part of the most amplified mode is very close to zero, which means it is the nonoscillatory mode. The superposition of this mode on the basic flow demonstrates the rotation of the flowfield around the major axis of the spheroid. Considering that the symmetric plane in Fig. 11 has a degree of freedom for the azimuth angle, the mode which corresponds to the rotation around the axis is expected to be a neutral stable mode.

Now, we focus on the second largest mode. The imaginary part of the second largest mode is not zero. This mode is the oscillatory mode. The real part of the second most amplified mode is estimated to become zero around $Re_{C2} \sim 6.6 \times 10^3$. The frequency of the second most amplified mode is calculated as

$$f = \Im\left(\lambda^{(A)}\right)\big/2\pi \qquad (23)$$

where $\lambda^{(A)}$ is calculated by Eq. (24). The frequency is normalized by the freestream velocity and the length of the major axis of the spheroid. If the argument of $\lambda^{(B)}$ is smaller than π, the eigenvalue $\lambda^{(A)}$ becomes 2.1, and the frequency becomes $f = 0.33$ in the case $Re = 6.5 \times 10^3$. However, we cannot deny the possibility that the argument of $\lambda^{(A)}$ is not the principal value. Considering that the logarithm is a multivalued function, Eq. (22) is expressed as

$$\lambda^{(A)} = \left\{\log\left|\lambda^{(B)}\right| + i\mathrm{Arg}\lambda^{(B)} + 2n\pi i\right\}\big/T, \qquad n \in \mathbf{Z} \quad (24)$$

If the value n of Eq. (24) is -1, then the frequency is $f = 0.67$. If the value n is 1, then the frequency is $f = 1.33$. To confirm the value of the frequency, the numerical computation of the flowfield is conducted with a supercritical condition ($Re = 7.0 \times 10^3$). The result of the frequency analysis, which is adapted to the time history of the lift-to-drag ratio, is shown in Fig. 17. We can recognize a
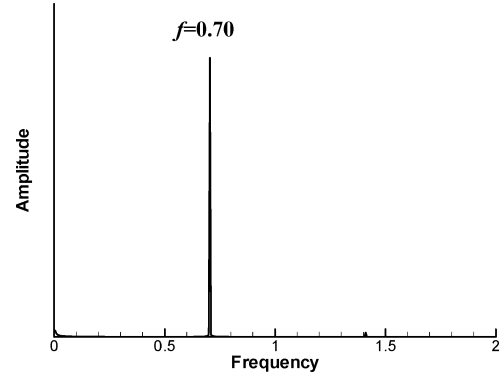

Fig. 17 Frequency analysis of the side-force-to-drag ratio ($Re = 7.0 \times 10^3$, angle of attack = 0 deg).
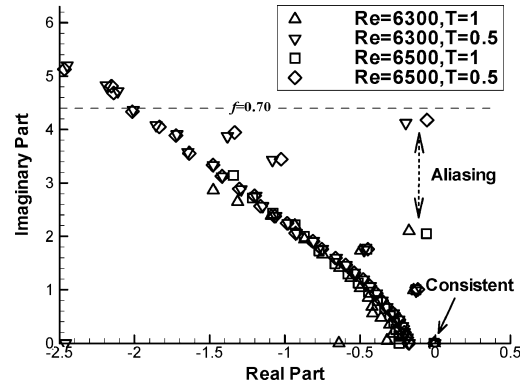

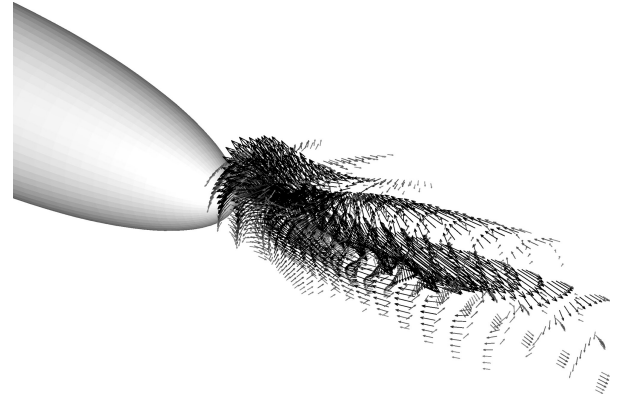**Fig. 18 Dependence of the imaginary part of eigenvalues on T (angle of attack = 0 deg).**

Fig. 19 Velocity disturbance of the oscillatory mode (angle of attack = 0 deg, fine grid).

sharp peak at $f = 0.70$. Then the frequency of the oscillatory mode is determined to be $f = 0.67$.

If we set several types of T, we can find out the aliasing error. Here, we set T as 0.5, and the stability is calculated in the same way. The result is shown in Fig. 18. To retain the total computational time, M is set as 80. The real part and imaginary part of almost all modes are the same except for the second most amplified mode. The probable values of the frequency of the second most amplified mode become 0.67, 1.33, 2.67, etc. The possibility of $f = 0.33$ is denied.

To check the dependency of the value of frequency on the grid resolution, computational study of the flowfield is also conducted using a fine grid (see Fig. 4). The result for $Re = 7.0 \times 10^3$ shows a peak at frequency $f = 0.59$, whose value is smaller than that for the normal grid. The most amplified mode of the stability analysis result at $Re = 6.5 \times 10^3$ is shown in Fig. 19. The amplification factor of this mode is negative. The critical value from nonoscillatory flow to oscillatory flow exists between 6.5×10^3 and 7.0×10^3. The oscillatory mode is planar symmetric with respect to the plane
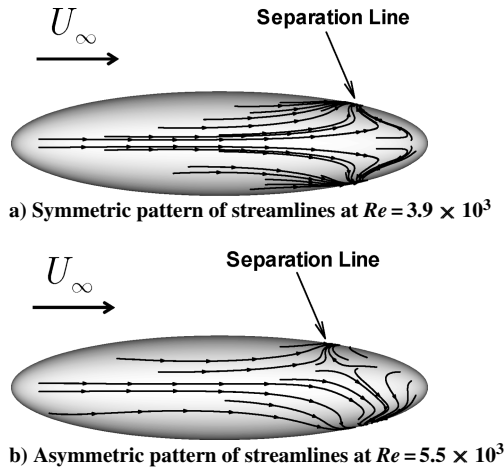
a) Symmetric pattern of streamlines at $Re = 3.9 \times 10^3$

b) Asymmetric pattern of streamlines at $Re = 5.5 \times 10^3$

Fig. 20   Leeside view of surface streamlines (spheroid, angle of attack = 10 deg).

of symmetry. Therefore, if the Reynolds number is a little higher than the critical value Re_{C2} and the magnitude of the disturbance is small, we can observe a planar-symmetric oscillation.

It is not easy to extract the perturbation of the flowfield as shown in Fig. 19 from a CFD result. The result of the stability analysis implies that the grid resolution is not enough to resolve the intricate structure of the oscillatory flowfield clearly. Future studies (promising that more powerful computers will be available) will clarify the detailed structure of the oscillatory mode using a sufficiently fine grid enough to resolve the mode.

2.   Angle of Attack of 10 deg

The flow around a spheroid at an angle of attack also becomes steady asymmetric in a certain range of Reynolds number. Figure 20a shows the leeside view of the surface streamlines of the flow at $Re = 3.9 \times 10^3$ and an angle of attack of 10 deg. The pattern of the surface streamlines is symmetric. However, the surface streamlines of the flow at $Re = 5.5 \times 10^3$, which are shown in Fig. 20b, show an asymmetric pattern. The asymmetry of the flowfield is also confirmed by the fact that the side force is generated on the body. The magnitude of the side force is about 5% of the axial force. The stationary solution of the CFD result is selected as the basic flow for the stability analysis. Figure 21a shows the eigenvalues on the complex plane. The imaginary part of the eigenvalue whose real part is the largest is zero. When the Reynolds number becomes larger than the critical value Re_{C1}, which is estimated to be 4.05×10^3, the amplification factor of the nonoscillatory asymmetric mode becomes positive. The flow changes from nonoscillatory symmetric flow to nonoscillatory asymmetric flow. The critical value Re_{C1} calculated using the fine grid is 3.86×10^3. This value is closer to the critical value at a zero attack angle, which is around 3.83×10^3. In either case, we can conclude that the steady asymmetric (or nonaxisymmetric) flow is observed if the Reynolds number is approximately larger than 4.0×10^3.

We cannot deny the possibility that the nonoscillatory asymmetric flow appeared by some numerical reason. Experimental study is necessary for the confirmation of the appearance of the steady asymmetric flow. In this study, experimental study is also conducted to demonstrate the appearance of the steady asymmetric flow, which is described in Sec. IV.

The results of the stability analysis at $Re = 5.4 \times 10^3$, 5.5×10^3, and 5.45×10^3 are shown in Fig. 21b. The stationary solutions of CFD, which show an asymmetric pattern in the surface streamlines (similar to Fig. 20b), are used as the basic flows. The result shows that the real part of the eigenvalue is smaller than zero for all of the modes. The asymmetric flow at $Re = 5.5 \times 10^3$ is shown to be stable. In the case of $Re = 5.5 \times 10^3$, the imaginary part of the most amplified mode is not zero. That is to say, the oscillatory mode is least decayed. The frequency of the most amplified mode is 0.11. The flowfield changes from steady flow to oscillatory flow when the
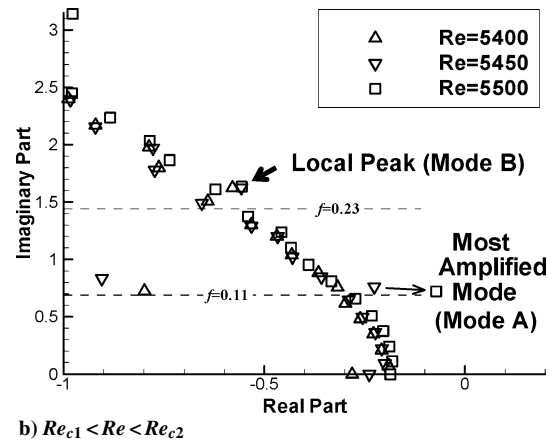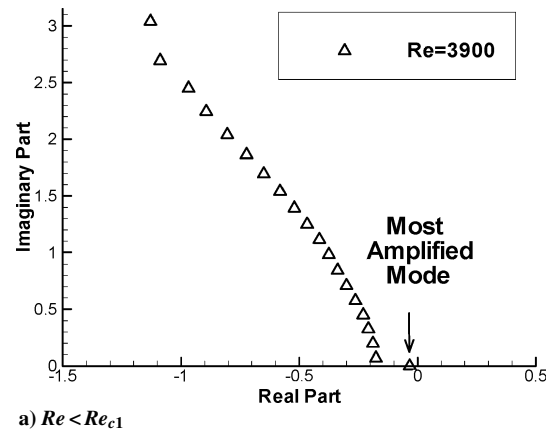

a) $Re < Re_{c1}$

b) $Re_{c1} < Re < Re_{c2}$

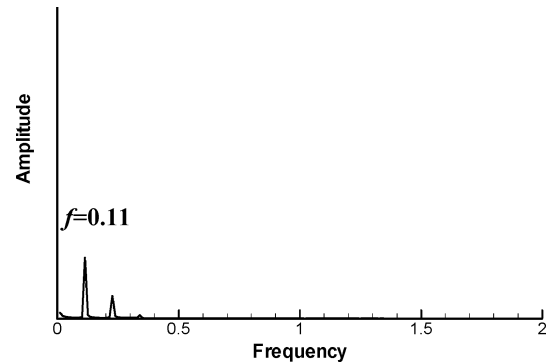**Fig. 21   Eigenvalues on a complex plane (spheroid, angle of attack = 10 deg).**

Fig. 22   Frequency analysis of the side force (angle of attack = 10 deg, $Re = 5.55 \times 10^3$).

Reynolds number becomes larger than the critical Reynolds number Re_{C2} which is estimated to be around 5.52×10^3. Figure 22 shows the power spectrum of the oscillatory side force at $Re = 5.55 \times 10^3$. A peak of the spectrum is observed at a frequency of 0.11. This value is consistent with the result of the stability analysis. A peak of the spectrum is also observed at a frequency of 0.23. In the result of the global stability analysis, a mode that has a frequency a little larger than 0.23 (Fig. 21) shows a local peak. In both mode, aliasing does not occur, because these frequencies are smaller than half the value of the sampling frequency $f/2 = (1/T)/2 = 0.5$.

Here, the mode with a frequency close to $f = 0.11$, and having the largest amplification factor, is named "mode A," and the mode with a frequency close to $f = 0.23$, and the amplification factor shows a local peak, is named "mode B." The velocity disturbances of modes A and B are plotted in Fig. 23. Mode A oscillates the velocity in the nearfield region more than in the far-field region, whereas mode B oscillates the velocity in the far-field region more than in the
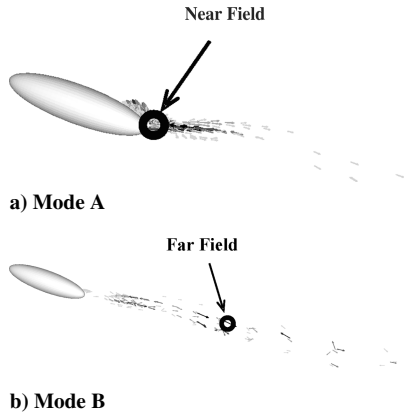
a) Mode A

b) Mode B

Fig. 23   Contour surface of the magnitude of velocity disturbance.

a) Near-field region
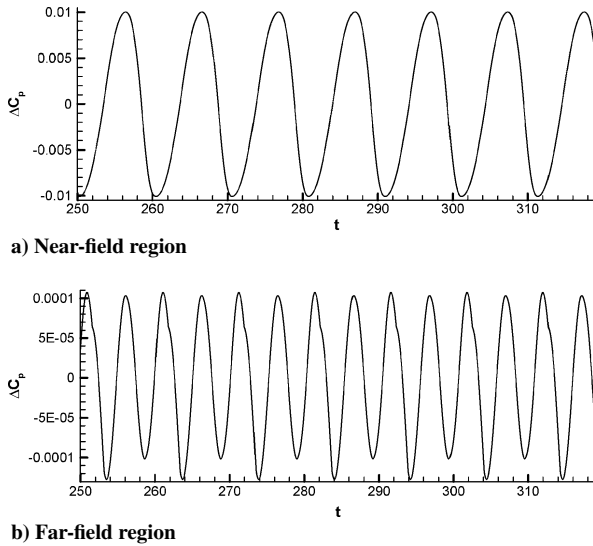

b) Far-field region

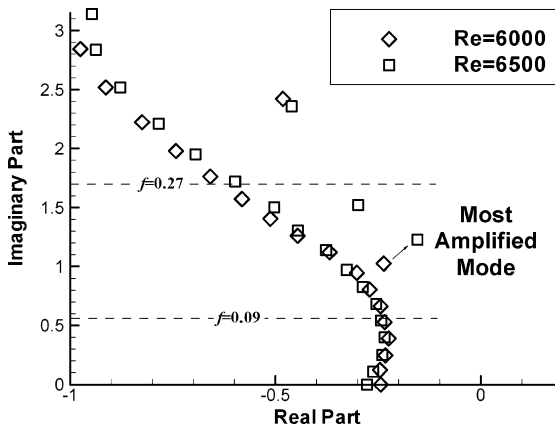Fig. 24   Time history of the pressure.

Fig. 25   Eigenvalues on a complex plane (spheroid, angle of attack = 10 deg, fine grid).

near-wake region. Then, time histories of the of the CFD result in the near-field and far-field regions is checked. Though the velocity of these regions include both frequencies, the frequency of the pressure is around 0.1 at the near-field region (Fig. 24a) and around 0.2 at the far-field region (Fig. 24b). The difference in the frequency of the pressure in the near-field region and the far-field region is expected to be explained by the mode of the three-dimensional global linear stability analysis.

The stability analyses are also conducted using the fine grid, which is shown in Fig. 25. The amplification factor of the most amplified mode is negative in both the $Re = 6.0 \times 10^3$ and the $Re = 6.5 \times 10^3$ cases. This result indicates that nonoscillatory asym-
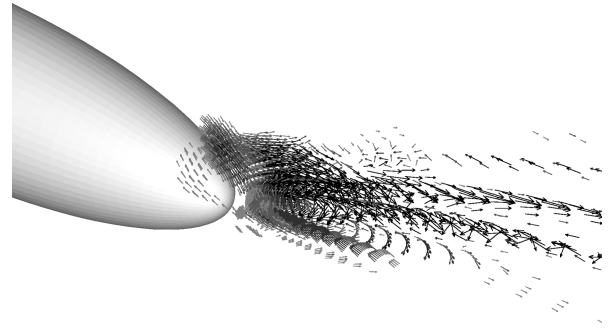

Fig. 26   Velocity disturbance of the oscillatory mode (angle of attack = 0 deg, fine grid).

metric flowfield remains stable when the Reynolds number is higher than 6.5×10^3. The CFD result of the $Re = 7.0 \times 10^3$ case shows an oscillatory flowfield. The most dominant frequency is $f = 0.27$, and the second most dominant frequency is $f = 0.09$. The critical value Re_{C2} is considered to exist between $Re = 6.5 \times 10^3$ and 7.0×10^3. The region that the most amplified mode is dominant in, is the nearfield region. The amplification factor of the oscillatory mode whose frequency is close to 0.09 is a local maximum. The region that this mode is dominant in, is the far-field region. The velocity disturbance of the most amplified oscillatory mode demonstrates an asymmetric configuration with respect to the plane of symmetry. Therefore, even in the supercritical condition, an averaged flowfield of the oscillatory flow remains asymmetric. The spatial asymmetry is sustained after the temporal instability sets in.

A detailed check of the result of the stability analysis lets us notice that the most amplified mode calculated by using a normal grid demonstrates spatial oscillation of the velocity disturbance. In other words, the direction of the velocity disturbance alternates at every other grid point (Fig. 26). Insufficiency of the spatial resolution of the normal grid seems to generate this nonphysical oscillation, and the critical value Re_{C2} becomes lower. Therefore, the critical Reynolds number for the oscillatory flow is estimated to exist between $Re = 6.5 \times 10^3$ and $Re = 7.0 \times 10^3$.

3.   Effect of Length-to-Diameter Ratio

The flow around a spheroid whose length-to-diameter ratio is 6:1 is also calculated. When the angle of attack is 30 deg, the flow becomes steadily asymmetric in a narrow range of Reynolds number around 7.1×10^3. However, the side force is negligibly small. When the length-to-diameter ratio becomes larger than 4:1, the range of the Reynolds numbers in which the steady asymmetric flow is observed becomes narrower, and the difference between Re_{C1} and Re_{C2} becomes smaller.

IV.   Experimental Results

To confirm the existence of steady asymmetric flow around a spheroid in a certain range of Reynolds number and attack angle, experimental research was also carried out. In this study, we focused on the appearance of the nonoscillatory asymmetric flowfield. Considering that the Reynolds number was on the order of 10^4, the experimental model and freestream velocity became small. This indicates that the measurement of the drag and side force is very difficult because these physical quantities are small. Therefore, we decided to conduct a flow visualization technique.

A Göttingen-type wind tunnel at the Department of Aeronautics and Astronautics at the University of Tokyo was used to observe the asymmetric flow around a spheroid at angle of attack 10 deg. The diameter of the test section was 1.5 m. The length and diameter of the spheroidal model were 80 and 20 mm, respectively. As shown in Fig. 27a, the spheroidal model was supported by a sting with a diameter of 2 mm. A thin metallic pipe with a diameter of 1.4 mm was placed parallel to the sting. A laser sheet was used for the flow visualization. Tracers generated by the fog generator are injected into the recirculation region through this pipe. To take pictures of the recirculation region, a CCD camera was placed in the center
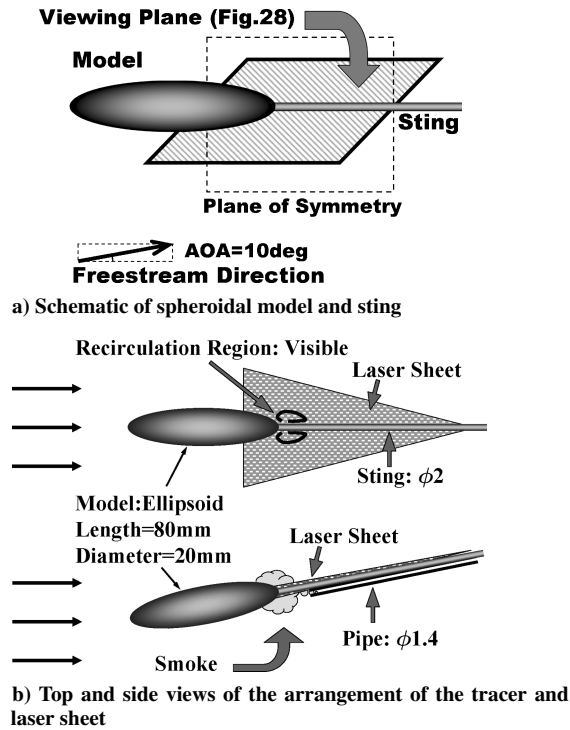
a) Schematic of spheroidal model and sting

b) Top and side views of the arrangement of the tracer and laser sheet

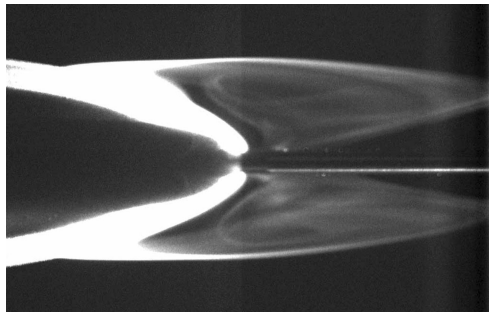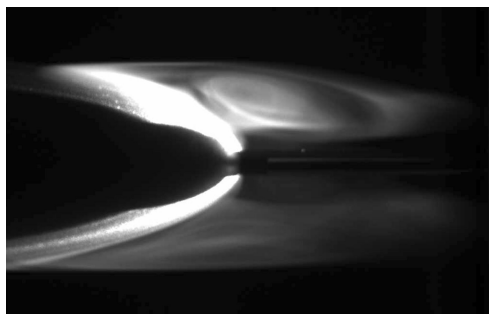**Fig. 27   Schematic of the experimental setup.**

a) Symmetric pattern of flow visualization at $Re \sim 3.5 \times 10^3$

b) Asymmetric pattern of flow visualization at $Re \sim 6.5 \times 10^3$

Fig. 28   Experimental result of flow visualization around a spheroid supported by sting.

of the wind tunnel. The time of exposure was set at 300 ms. The angle of attack was set at 10 deg. First, the velocity of the flow was set to the condition $Re \sim 3.5 \times 10^3$. In this case, the flowfield was considered to demonstrate a symmetric pattern from the discussion of Sec. III.B.2. Figure 28a shows the result of the flow visualization. The pattern of the recirculation region was symmetric. Then the velocity of flow was changed to the condition of $Re \sim 6.5 \times 10^3$. In this case, the flowfield would show an asymmetric pattern. The result of the flow visualization, which is shown in Fig. 28b, demonstrates an asymmetric pattern in the recircular region.

To compare the experimental results with numerical results, the flow around a spheroid with a sting was also calculated. The result
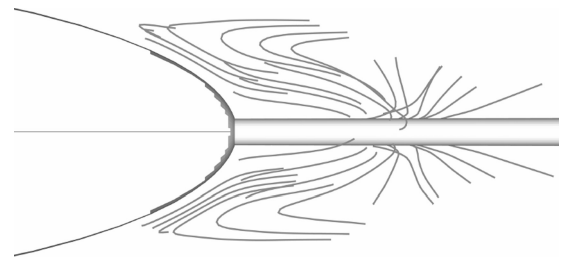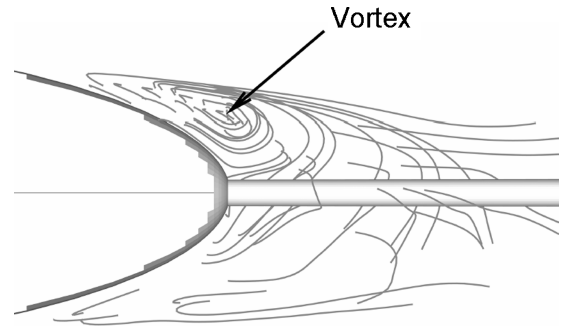

a) Symmetric pattern of streamline at $Re = 4.0 \times 10^3$

b) Asymmetric pattern of streamline at $Re = 6.0 \times 10^3$

Fig. 29   Numerical result of flow around spheroid with sting.

of the numerical computation shows that the flow at $Re = 4.0 \times 10^3$ is symmetric. The cross-sectional view of the plane that corresponds to the viewing plane of Fig. 27a is plotted in Fig. 29a. The computed streamlines at $Re = 6.0 \times 10^3$, which are shown in Fig. 29b, demonstrate the asymmetric pattern. On the upper side of Fig. 29b, a vortex structure is observed. The experimental result shows a vortex-resembling structure on the upper side of Fig. 28b.

To check that this asymmetric flow is oscillatory or steady, several pictures were taken at different times. The smoke pattern was consistently similar to the pattern shown in Fig. 28. We can conclude that the onset of the steady asymmetric flow around a spheroid at attack angle 10 deg is experimentally confirmed.

V.   Conclusions

A computational code for the three-dimensional global linear stability analysis of incompressible flows has been developed. This code is applied to the flow around a spheroid at incidence, and the stability of the flowfield is calculated. Using the result of the stability analysis, we can explain the appearance of a nonoscillatory nonaxisymmetric or asymmetric flowfield:

1) In the case of attack angle 0 deg, the nonoscillatory, nonaxisymmetric flowfield is observed at the range of Reynolds numbers around 4.0×10^3 to 7.0×10^3. The amplification factor of the nonoscillatory mode becomes positive at lower Reynolds numbers than the critical Reynolds number from nonoscillatory flow to oscillatory flow. At higher Reynolds numbers, the amplification factor of the oscillatory mode becomes zero. Therefore, steady axisymmetric, steady nonaxisymmetric, and oscillatory patterns successively appear according to the increase in the Reynolds number.

2) The transition from steady symmetric flow to steady asymmetric flow also occurs in nonzero attack angle. For attack angles other than 0 deg, steady symmetric, steady asymmetric, and oscillatory patterns successively appear according to the increase in the Reynolds number. The range of the Reynolds number where the nonoscillatory asymmetric flow is observed is around 4.0×10^3 to 7.0×10^3.

3) In the case in which the length-to-diameter ratio is 6:1, steady asymmetric flow is observed in a narrow range of Reynolds numbers. However, the side force is very small and negligible. The Reynolds number range in which the steady asymmetric flow becomes stable depends on the length-to-diameter ratio.

4) For confirmation of the appearance of nonoscillatory asymmetric flow, experimental study was also conducted. A flow visualization technique was used to clarify the asymmetric flowfield in

the low-Reynolds-number region. The pattern of the recirculation region shows in asymmetric configuration when the Reynolds number is around 6.5×10^3, whereas it is symmetric when the Reynolds number is around 3.5×10^3.

References

[1] Kubota, H., Arai, I., and Matsuzaka, M., "Flat Spin of Slender Bodies at High Angles of Attack," *Journal of Spacecraft and Rockets*, Vol. 20, No. 2, 1983, pp. 108–114.

[2] Magarvey, R. H., and Bishop, R. L., "Transition Ranges for Three-Dimensional Wakes," *Canadian Journal of Physics*, Vol. 39, No. 10, 1961, pp. 1418–1422.

[3] Ormières, D., and Provansal, M., "Transition to Turbulence in the Wake of a Sphere," *Physical Review Letters*, Vol. 83, No. 1, 1999, pp. 80–83.

[4] Johnson, T. A., and Patel, V. C., "Flow Past a Sphere up to a Reynolds Number of 300," *Journal of Fluid Mechanics*, Vol. 378, 1999, pp. 19–70.

[5] Theofilis, V., "Advances in Global Linear Instability Analysis of Non-parallel and Three-Dimensional Flows," *Progress in Aerospace Sciences*, Vol. 39, No. 4, 2003, pp. 249–315.

[6] Huerre, P., and Monkewitz, P. A., "Local and Global Instabilities in Spatially Developing Flows," *Annual Review of Fluid Mechanics*, Vol. 22, 1990, pp. 473–537.

[7] Natarajan, R., and Acrivos, A., "The Instability of the Steady Flow past Spheres and Disks," *Journal of Fluid Mechanics*, Vol. 254, 1993, pp. 323–344.

[8] Ghidersa, B., and Dušek, J., "Breaking of Axisymmetry and Onset of Unsteadiness in the Wake of a Sphere," *Journal of Fluid Mechanics*, Vol. 423, 2000, pp. 33–69.

[9] Wang, K. C., Zhou, H. C., Hu, C. H., and Harrington, S., "Three-Dimensional Separated Flow Structure over Prolate Spheroids," *Proceedings of the Royal Society of London, Series A: Mathematical and Physical Sciences*, Vol. 429, No. 1876, 1990, pp. 73–90.

[10] Han, T., and Patel, V. C., "Flow Separation on a Spheroid at Incidence," *Journal of Fluid Mechanics*, Vol. 92, 1979, pp. 643–657.

[11] Costis, C. E., Hoang, N. T., and Telionis, D. P., "Laminar Separating Flow over a Prolate Spheroid," *Journal of Aircraft*, Vol. 26, No. 9, 1989, pp. 810–816.

[12] Nishikawa, N., Ishide, T., and Kida, S., "Surface Flow Patterns on Blunt Bodies," *Fluid Dynamics of High Angle of Attack*, edited by R. Kawamura and Y. Aihara, Springer-Verlag, Berlin, 1992, pp. 213–221.

[13] Chiba, S., "Global Stability Analysis of Incompressible Viscous Flow," *Journal of Japan Society of Computational Fluid Dynamics*, Vol. 7, No. 1, 1998, pp. 20–48 (in Japanese).

[14] Eriksson, L. E., and Rizzi, A., "Computer-Aided Analysis of the Convergence to Steady State of Discrete Approximations to the Euler Equations," *Journal of Computational Physics*, Vol. 57, No. 1, 1985, pp. 90–128.

[15] Arnoldi, W. E., "The Principle of Minimized Iterations in the Solution of the Matrix Eigenvalue Problem," *Quarterly of Applied Mathematics*, Vol. 9, No. 1, 1951, pp. 17–29.

[16] Harlow, F. H., and Welch, J. E., "Numerical Calculation of Time-Dependent Viscous Incompressible Flow of Fluid with Free Surface," *Physics of Fluids*, Vol. 8, No. 12, 1965, pp. 2182–2189.

[17] Greenspan, D., "Numerical Studies of Prototype Cavity Flow Problems," *Computer Journal*, Vol. 12, No. 1, 1969, pp. 88–93.

[18] Kawamura, T., and Kuwahara, K., "Computation of High Reynolds Number Flow around Circular Cylinder with Surface Roughness," AIAA Paper 84-0340, Jan. 1984.

A. Karagozian
Associate Editor